

Persistence of magnetic field driven by relativistic electrons in a plasma

A. Flacco^{1*}, J. Vieira², A. Lifschitz¹, F. Sylla^{1†}, S. Kahaly^{1†}, M. Veltcheva¹, L. O. Silva² and V. Malka¹

The onset and evolution of magnetic fields in laboratory and astrophysical plasmas is determined by several mechanisms¹, including instabilities^{2,3}, dynamo effects^{4,5} and ultrahigh-energy particle flows through gas, plasma^{6,7} and interstellar media^{8,9}. These processes are relevant over a wide range of conditions, from cosmic ray acceleration and gamma ray bursts to nuclear fusion in stars. The disparate temporal and spatial scales where each process operates can be reconciled by scaling parameters that enable one to emulate astrophysical conditions in the laboratory. Here we unveil a new mechanism by which the flow of ultra-energetic particles in a laser-wakefield accelerator strongly magnetizes the boundary between plasma and non-ionized gas. We demonstrate, from time-resolved large-scale magnetic-field measurements and full-scale particle-in-cell simulations, the generation of strong magnetic fields up to 10–100 tesla (corresponding to nT in astrophysical conditions). These results open new paths for the exploration and modelling of ultrahigh-energy particle-driven magnetic-field generation in the laboratory.

Strong cosmic magnetization requires ultrahigh-energy particle flows. These non-thermal particle streams can be produced¹⁰ by statistical acceleration processes, such as shock^{11,12} and Fermi acceleration¹³, and by direct particle acceleration mechanisms in strong wave fields, such as those found in pulsars¹⁴. In addition to direct astronomical observations, the physical processes occurring when these mechanisms take place may also be explored in the laboratory. For instance, the conditions for the onset of statistical acceleration mechanisms through collisionless shocks in the laboratory have been investigated theoretically¹⁵. Direct cosmic acceleration can also be explored in the laboratory through laser-driven plasma wakefields^{16–18}. Here we show that the non-thermal particle flows produced in a laser-wakefield accelerator (LWFA; refs 19–21) can strongly magnetize the plasma and the plasma–neutral gas boundary. This observation is also the first showing that the strong magnetization occurring at the flow of energetic particles from ionized to non-ionized interstellar material can be reproduced in the laboratory.

A LWFA uses short and intense laser pulses to drive large-amplitude plasma waves. In the LWFA scheme, the laser ponderomotive force excites ultra-relativistic, large-amplitude plasma waves where electrons can be trapped and accelerated to high energies.

In our LWFA experiment the plasma is created in a helium gas jet produced in vacuum by a nozzle of 400 μm in diameter^{22,23}. The gas leak reaches, at its centre, a neutral density of $n_A = 3.5 \times 10^{19}$ atoms cm^{-3} , which corresponds, when fully ionized, to an electronic density of $n_0 = 4\% n_c$ with $n_c = (2\pi c)^2 m_e \epsilon_0 / e^2 \lambda^2$

the critical density at $\lambda = 800$ nm, where c is the speed of light in vacuum, e and m_e , respectively, the electron charge and mass, and ϵ_0 the vacuum permittivity. A driver laser pulse of 30 fs in duration is focused perpendicularly to the gas jet direction by an off-axis parabolic reflector (Fig. 1a) to a transverse spot size of 8 μm full-width at half-maximum (FWHM), reaching a peak intensity of $I_0 = 3 \times 10^{19}$ W cm^{-2} . Because the laser power exceeds the critical power for relativistic self-focusing²⁴, the peak laser intensity in the plasma is further increased, which leads to the excitation of strongly nonlinear plasma waves that, at this density, are above the wave-breaking threshold. Moreover, the driver laser pulse duration is very close to the plasma period, hence the plasma waves are resonantly excited, which enhances the onset of wave breaking.

Wave breaking occurs at the transition between laminar and turbulent electron flows, when the plasma wave amplitude exceeds a given threshold. As the wave breaks, electrons thermalize while accelerating to relativistic energies, damping the amplitude of the plasma wave. Thus, wave breaking leads to non-thermal particle flows at relativistic energies that expand radially away from the laser axis, as they also move at relativistic velocities in the forward direction.

These non-thermal electrons expand radially, eventually reaching the plasma–neutral gas boundary, located where laser fields are not sufficiently high to ionize the background gas. As they propagate through the ionized medium, return currents are set up to balance the hot electron flow, preventing effective magnetic-field generation. These return currents appear only inside the plasma, where the gas is ionized. In the neutral gas region, however, there are no free charges that are capable of generating return currents to compensate for hot electron currents (impact ionization of neutral gas due to non-thermal electron propagation is negligible). Thus, hot electrons crossing the plasma–neutral gas boundary are able to generate strong fields that magnetize the neutral gas and the peripheral regions of the plasma cylinder. Although direct measurement of wave breaking is extremely challenging, the measured large-scale magnetic field is indirect evidence for its onset, because of the key role wave-breaking-produced electrons play in the field generation.

We demonstrate that this mechanism can produce strong magnetic fields scaling as $32\eta_{\text{hot}}(n_0 [10^{16} \text{ cm}^{-3}])^{1/2}$ T in the laboratory, where η_{hot} is the fraction of hot electrons to background plasma density n_0 . Thus, under astrophysical conditions, fields created by the same mechanism can reach amplitudes scaling as $320\eta_{\text{hot}}(n_0 [\text{cm}^{-3}])^{1/2}$ nT. Hot electrons here play the role of supra-thermal beams, as opposed to thermal beams, which are responsible for non-thermal radiation spectra and to strong magnetization in astrophysical scenarios.

¹Laboratoire d'Optique Appliquée, ENSTA-ParisTech, Ecole Polytechnique-ParisTech, CNRS UMR 7639, 828 Boulevard des Marechaux, 91762 Palaiseau CEDEX, France. ²GoLP/Instituto de Plasmas e Fusão Nuclear, Instituto Superior Técnico, Universidade de Lisboa, Lisbon 1049-001, Portugal. [†]Present addresses: SourceLAB SAS, 86 rue de Paris, 91400 Orsay, France (F.S.); ELI-ALPS, ELI-Hu Nkft, Dugonics ter 13, Szeged 6720, Hungary (S.K.).

*e-mail: alessandro.flacco@polytechnique.edu

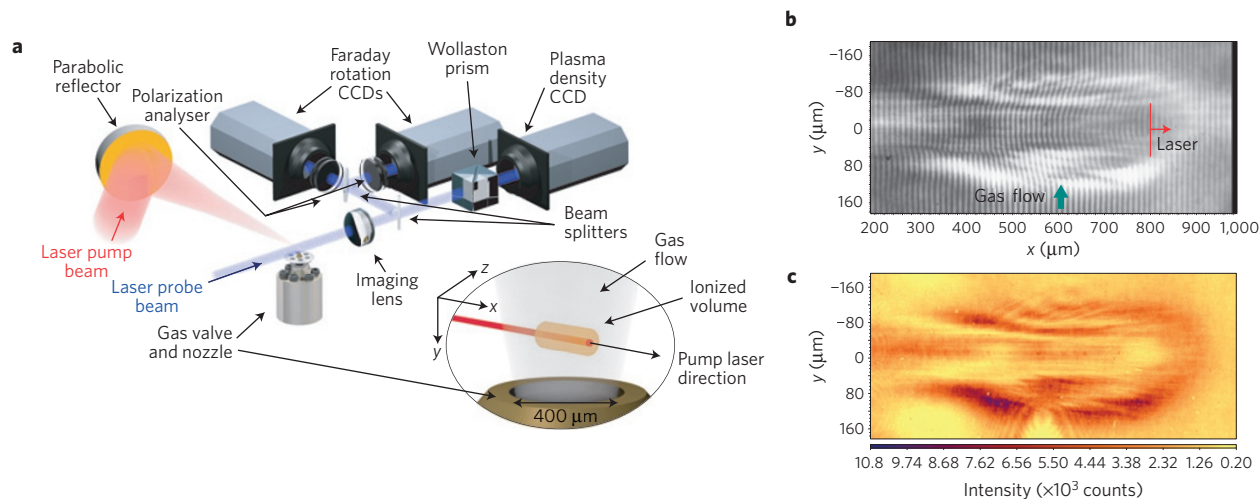


Figure 1 | Measurement of the electron density and magnetic field on propagation of an intense laser pulse through a dense gas jet. **a**, Scheme of the optical set-up, showing the laser pump beam (red) focused into the gas jet and the laser probe beam (blue) split multiple times after propagation through the plasma for simultaneous measurement of electron density and Faraday rotation. The probe beam propagates perpendicularly to the pump laser path, integrating the polar magnetic component and the density in the plasma. **b, c**, Images of the plasma while the laser propagates, at $t = 1.9$ ps. **b**, Interference map showing the integrated phase. **c**, One of the two simultaneous images recording the polarization rotation onto the intensity (false colours).

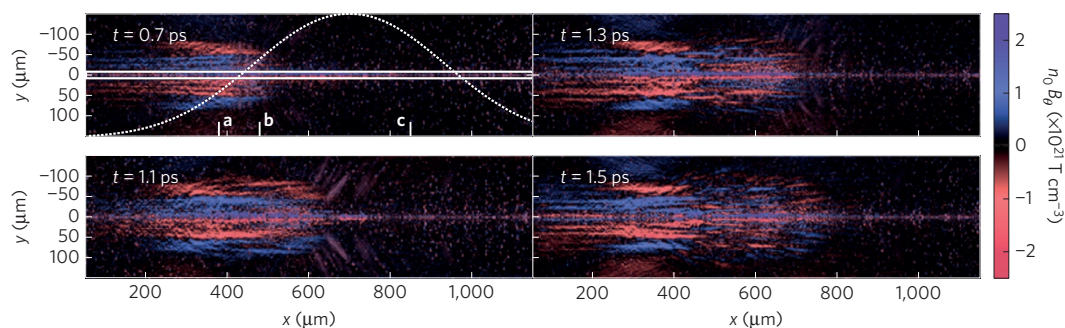


Figure 2 | Magnetization of the plasma at selected times. The laser pulse enters the gas area at $t = 0.3$ ps from the left hand side of the box. $t = 0.7$ ps, the bell-shaped plot represents the longitudinal neutral density profile in the gas jet, the highest density being $n_0 = 3.5 \times 10^{19}$ atoms cm^{-3} . The white continuous lines mark the laser beam waist size. The markers a, b, c in the top left panel correspond to the spatial positions in Fig. 3.

Our experiment provides the first time-resolved measurements of the spatial distribution of a magnetic field in a laser-plasma accelerator for the whole plasma volume and with a high temporal resolution. As the laser propagates through the gas target we observed strikingly complex magnetic structures, with several inversions of the field orientation at the plasma core. These observations are in excellent agreement with three-dimensional (3D) one-to-one particle-in-cell (PIC) simulations in OSIRIS (refs 25,26) capturing the global plasma dynamics and magnetic-field evolution over the entire gas jet, each taking several hundreds of thousands of CPU-hours (see Methods).

The laser interaction with the gas jet is thoroughly scanned at high temporal and spatial resolutions for electron density (via phase recording) and magnetic-field mapping. The plasma is probed by a single laser pulse of $t = 30$ fs in duration at $\lambda = 400$ nm. During its propagation in the plasma cylinder, polarization rotation and absolute dephasing are integrated and recorded on three separate charge-coupled device (CCD) cameras, as shown in Fig. 1a. The 3D density and magnetic maps are then reconstructed from the recorded information (see Methods). The delay between the driver and the probe pulses can be varied (with an accuracy of ~ 2 fs) to explore in time the propagation of the driver pulse and the evolution of the plasma. This pump-probe experiment permits us to freeze the plasma state to a high-resolution snapshot lasting for

only 30 fs and to follow its evolution. The validity of the magnetic-field measurement rests on the assumption that $\mathbf{B} \cdot \nabla n_0 = 0$ in the plasma cylinder, which is confirmed by simulations.

Snapshots of the spatial distribution of the magnetic field at selected times are shown in Fig. 2. Each image represents the symmetrized radial map of $(n_0 \mathbf{B})_\theta(r, x)$, the product between the polar component of the magnetic field and the local electron density, as reconstructed from the probe polarization maps. The laser pulse propagates from left to right. A polar magnetic field is observed in the trail of the laser pulse soon after entering the gas jet ($t = 0.7$ ps). From the density measurements we can infer a magnetic-field magnitude reaching 100 T. This field is positive in the plasma core ($r < 50 \mu\text{m}$) and changes in sign close to the radial border of the plasma ($r \sim 50 \mu\text{m}$). As we will see from simulations below, the inversion of the field direction at the boundary is a distinctive feature indicating an electron current passing through the plasma/gas boundary. These electrons (ultra-energetic particles in astrophysical scenarios) are relativistic and, although accelerated from the wave breaking, they are not trapped by the wakefield.

Figure 2 shows another striking feature, consisting of a strong magnetization of the plasma core. A large magnetic field is indeed expected close to the laser propagation axis, in the wakefield region. This field is created by the very high longitudinal wakefield current, which is not screened by the plasma. At a distance corresponding

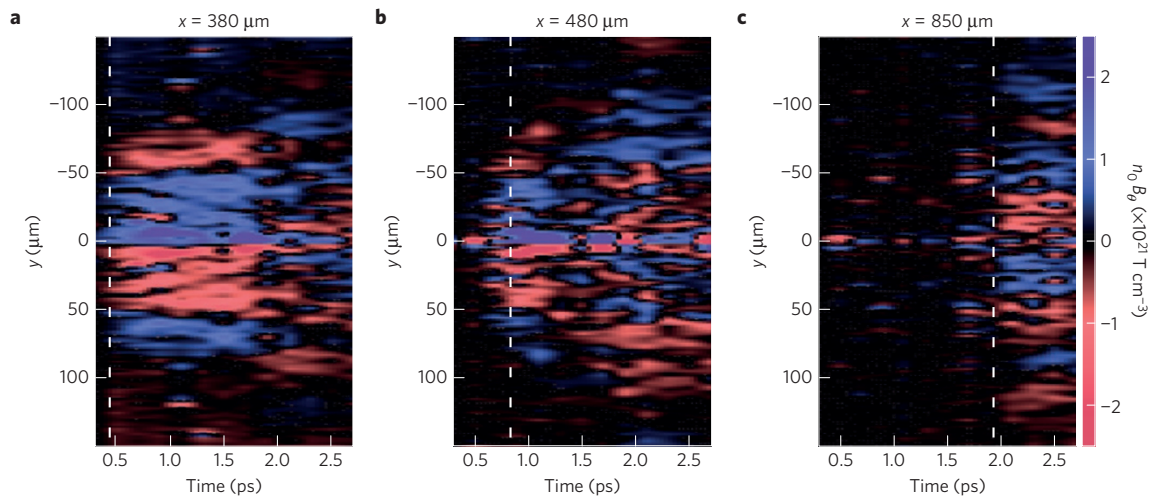


Figure 3 | Evolution in time of the magnetic field. **a–c**, Cross-sections at fixed planes along the laser propagation, the dotted vertical line represents the arrival of the laser front. Images are composed by extracting data from multiple laser shots at different delays, with increments of $\Delta t = 200$ fs. The positions refer to the corresponding markers in top left panel of Fig. 2.

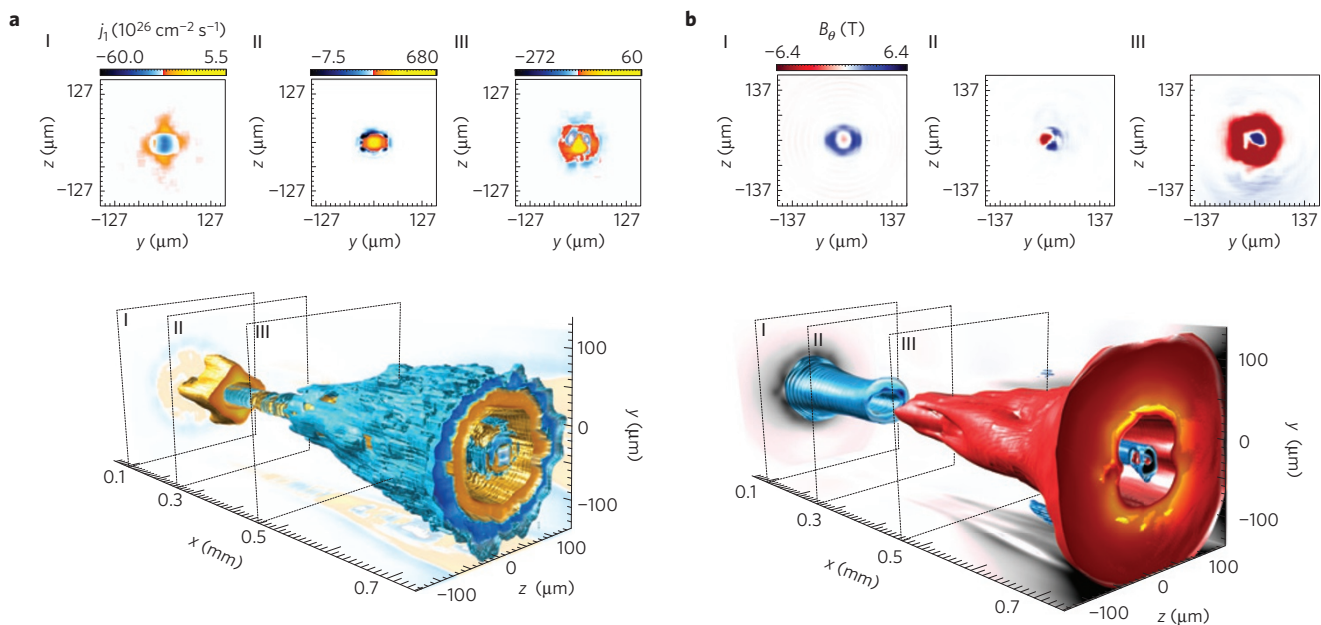


Figure 4 | Summarized results of a full 3D PIC simulation of the experiment. **a, b**, The final conditions of currents (**a**) and azimuthal magnetic field (**b**) in the plasma are shown after the laser pulse has propagated through the gas; three 2D cuts are shown for improved readability.

to the limit of the laser beam waist (that is, a few micrometres), a weak magnetic field survives (the bow wave magnetic field²⁷). Farther away from the axis, plasma return currents typically screen hot (non-thermal) electrons that expand radially from the wakefield (note that the main velocity component of these electrons is along x), thus no significant field is expected to survive up to the vicinity of the boundary. The experimental results suggest that in the plasma core the screening of hot electron current coming from the wakefield is not as efficient as expected.

The magnetic-field structure remains alike until $t = 1.1$ ps: starting from $t = 1.3$ ps, an island of reversed field starts building up close to the gas jet density peak ($x = 530 \mu\text{m}$), relatively far from the laser waist. At $t = 1.5$ ps (Fig. 2), this island has expanded longitudinally and radially, and a second island appears closer to the laser axis ($x = 580 \mu\text{m}$), at a larger radius. Simulations suggest that these islands are caused by the filamentation of the

wings of the laser pulse—that is, the laser energy surrounding the central spot.

Experiments showed several inversions of the magnetic-field orientation, as illustrated in Fig. 3. Several shots at different delays are used to compose a picture of the local evolution in time of the magnetic field. The temporal resolution in this figure is 200 fs. On entry into the gas (Fig. 3a) the laser propagation is accompanied by the formation of a positive poloidal magnetic field in the plasma core, which changes sign in the plasma boundary. The inner field component is consistent, in sign, with a negative current propagating with the laser pulse and remains stable for approximately 1.2 ps. Figure 3b shows the evolution in the region where the first island appears, $x = 480 \mu\text{m}$. At $t \sim 1.1$ ps the field sign is reversed in the plasma core, corresponding to the formation of the first island. This inversion lasts up to $t \sim 1.5$ ps. When the laser exits from the gas profile (Fig. 3c) a poloidal field is again formed, comparable

to Fig. 3a. At this time, however, the plasma core magnetization is opposite in sign to what was observed at the entrance.

Our experimental findings are confirmed by 3D PIC simulations run with parameters closely matching experimental laser and plasma conditions (see Methods). As it enters the gas, the laser ionizes the gas up to a radius of 100 μm away from the axis and excites weakly nonlinear plasma waves. Relativistic pulse self-focusing enhances the wakefield amplitude beyond the wave-breaking threshold after 400 μm of propagation. When wave breaking occurs, a fraction of the resulting hot electrons expand radially through the plasma.

The laser-driven plasma waves lead to complex longitudinal electron current structures in the ionized volume. Figure 4a shows the current structures at the end of the simulation, at $t = 2.67$ ps, where it is possible to distinguish between backward electron currents (blue) and forward electron currents (red). As electrons cross the plasma–neutral gas boundary an inner return current is set up, located at the boundary itself, at a variable radius in the range $r \lesssim 60\text{--}100 \mu\text{m}$. These currents, Fig. 4a, are the origin of the large-scale poloidal magnetic fields observed in Fig. 4b. Simulations also show that a small fraction of hot electrons at the plasma entrance ($x < 500 \mu\text{m}$) flow away from the laser in the backward direction. These are indicated by the red structures surrounding a blue core ($r \gtrsim 60 \mu\text{m}$) in Fig. 4a I. For $x > 500 \mu\text{m}$ most of the hot electrons are accelerated in the forward direction, leading to the outer forward current structures (blue) in Fig. 4a II and III.

Return currents electrons propagate forward at the leading edge of the gas profile (Fig. 4a I) and backward for the remainder of the gas jet length (Fig. 4a II,III). Because hot electrons flow in opposite directions for $x < 500 \mu\text{m}$ (Fig. 4b I) and for $x > 500 \mu\text{m}$ (Fig. 4b III), the sign of the magnetic field changes in these regions. The transition at $x \simeq 500 \mu\text{m}$ is shown in Fig. 4b II, which illustrates the poloidal magnetic field corresponding to the longitudinal currents shown in Fig. 4a. This transition to a richer current structure around $x \simeq 500 \mu\text{m}$ is confirmed by experimental observation (for example, Figs 2 and 3b).

The large-scale magnetic field that surrounds the plasma around $|y| \simeq 60\text{--}100 \mu\text{m}$ reaches amplitudes that are in fair agreement with experimental measurements ($n_0 B_z \simeq 10^{21} \text{ T cm}^{-3}$).

An estimate of the poloidal magnetic-field amplitude can then be determined considering the return currents at the plasma–gas interface. Using Ampère’s law to estimate the amplitude of the resulting azimuthal magnetic field (B_θ) in cylindrical symmetry gives

$$\int \mathbf{B} \cdot d\mathbf{l} \simeq 2\pi r B_\theta = (4\pi/c) \int \mathbf{j} \cdot d\mathbf{S} = \mu_0 \int \mathbf{j}_z \cdot d\mathbf{S}$$

where r is the distance to the axis, $d\mathbf{l}$ and $d\mathbf{S}$ are the line and surface elements for the integrations and μ_0 is the magnetic permeability of the vacuum. For relativistic hot electrons moving at velocity c longitudinally, $\mathbf{j} \simeq ec(\eta_{\text{hot}} n_0) \mathbf{e}_z$, where e is the elementary charge and \mathbf{e}_z is the unit vector pointing in the z direction. When r is greater than the plasma radius r_p , the return current density flux is $\eta_{\text{hot}} e n_0 4\pi^2 [r_p^2 - (r_p - \Delta)^2] \simeq 4\pi^2 c e n_0 \eta_{\text{hot}} r_p \Delta$, where $\Delta \simeq c/\omega_p \ll r$ is the thickness of the plasma the return currents are set up in, hence $B_\theta \simeq 4\pi e n_0 c \eta_{\text{hot}} (r_p/r)(c/\omega_p)$. The typical generated magnetic fields are of the order of B_θ [T] $\simeq 32\eta_{\text{hot}} \sqrt{n_0} [10^{16} \text{ cm}^{-3}]$ for $r \simeq r_p$. Considering $\eta_{\text{hot}} \simeq 0.05$ (taken from simulations) and $n_0 = 7 \times 10^{19} \text{ cm}^{-3}$, we obtain $B_\theta \simeq 80$ T, which is consistent with the simulation results. In astrophysical scenarios, the amplitude of the cosmic magnetic fields generated by this mechanism can be extrapolated to $320 \eta_{\text{hot}} \sqrt{n_0} [\text{cm}^{-3}]$ nT. This is consistent with the magnetization in the interstellar and extragalactic media, both of the order of 0.1–1 nT for densities of ~ 1 particle cm^{-3} (interstellar medium) and $10^{-2}\text{--}10^{-4}$ particles cm^{-3} (extragalactic medium)²⁸ considering η_{hot} between $\eta_{\text{hot}} \sim 0.01$ (as for the conditions of the experiment and

simulations) and $\eta_{\text{hot}} \sim 1$ (which may be obtained by using a smaller plasma radius and higher laser intensities).

The presented magnetic field increases with the background plasma density and the fraction of hot (supra-thermal) particles as $\eta_{\text{hot}} n_0^{1/2}$: this is a key scaling parameter which relates these results to astrophysical conditions. The ratio η_{hot} can be controlled by changing the volume of the plasma, which plays the role of the ionized interstellar (or extragalactic) region, and by the laser intensity, which plays the role of a central engine accelerating supra-thermal particles. Hence, by controlling the plasma and the parameters that define the magnetic-field amplitude it will be possible to quantitatively explore the magnetization of the interstellar/extragalactic magnetic fields in scaled experiments.

Methods

Methods and any associated references are available in the [online version of the paper](#).

Received 1 July 2014; accepted 16 March 2015;
published online 20 April 2015

References

- Kulsrud, R. & Zweibel, E. B. On the origin of cosmic magnetic fields. *Rep. Prog. Phys.* **71**, 046901 (2008).
- Medvedev, M. V. & Loeb, A. Generation of magnetic fields in the relativistic shock of γ -ray burst sources. *Astrophys. J.* **526**, 697–706 (1999).
- Silva, L. O. *et al.* Interpenetrating plasma shells: Near-equipartition magnetic field generation and nonthermal particle acceleration. *Astrophys. J. Lett.* **596**, L121 (2003).
- Brandenburg, A., Sokoloff, D. & Subramanian, K. Current status of turbulent dynamo theory. *Space Sci. Rev.* **169**, 123–157 (2012).
- Kulsrud, S. W. & Anderson, R. M. The spectrum of random magnetic fields in the mean field dynamo theory of the Galactic magnetic field. *Astrophys. J.* **396**, 606–630 (1992).
- Robinson, A. P. L. & Sherlock, M. Magnetic collimation of fast electrons produced by ultraintense laser irradiation by structuring the target composition. *Phys. Plasmas* **14**, 083105 (2007).
- Bell, A. R. & Kingham, R. J. Resistive collimation of electron beams in laser-produced plasmas. *Phys. Rev. Lett.* **91**, 035003 (2003).
- Miniati, F. & Bell, A. R. Resistive magnetic field generation at Cosmic Dawn. *Astrophys. J.* **729**, 73 (2011).
- Gregori, G. *et al.* Generation of scaled protogalactic seed magnetic fields in laser-produced shock waves. *Nature* **481**, 480–483 (2012).
- Hillas, A. M. The origin of ultra-high-energy cosmic rays. *Ann. Rev. Astron. Astrophys.* **22**, 425–444 (1984).
- Spitkovsky, A. Particle acceleration in relativistic collisionless shocks: Fermi process at last? *Astrophys. J. Lett.* **682**, L5 (2008).
- Martins, S. F., Fonseca, R. A., Silva, L. O. & Mori, W. B. Ion dynamics and acceleration in relativistic shocks. *Astrophys. J. Lett.* **695**, L189 (2009).
- Fermi, E. On the origin of the cosmic radiation. *Phys. Rev.* **75**, 1169–1174 (1949).
- Gunn, J. E. & Ostriker, J. P. Acceleration of high-energy cosmic rays by pulsars. *Phys. Rev. Lett.* **22**, 728–731 (1969).
- Fiuza, F., Fonseca, R. A., Tonge, J., Mori, W. B. & Silva, L. O. Weibel-instability-mediated collisionless shocks in the laboratory with ultraintense lasers. *Phys. Rev. Lett.* **108**, 235004 (2012).
- Rosenzweig, J. B. Trapping, thermal effects, and wave breaking in the nonlinear plasma wake-field accelerator. *Phys. Rev. A* **38**, 3634–3642 (1988).
- Chen, P., Tajima, T. & Takahashi, Y. Plasma wakefield acceleration for ultrahigh-energy cosmic rays. *Phys. Rev. Lett.* **89**, 161101 (2002).
- Chang, F.-Y., Chen, P., Lin, G.-L., Noble, R. & Sydora, R. Magnetowave induced plasma wakefield acceleration for ultrahigh energy cosmic rays. *Phys. Rev. Lett.* **102**, 111101 (2009).
- Malka, V. *et al.* Electron acceleration by a wake field forced by an intense ultrashort laser pulse. *Science* **298**, 1596–1600 (2002).
- Modena, A. *et al.* Electron acceleration from the breaking of relativistic plasma waves. *Nature* **377**, 606–608 (1995).
- Walton, B. *et al.* Measurements of magnetic field generation at ionization fronts from laser wakefield acceleration experiments. *New J. Phys.* **15**, 025034 (2013).
- Sylla, F., Veltcheva, M., Kahaly, S., Flacco, A. & Malka, V. Development and characterization of very dense submillimetric gas jets for laser-plasma interaction. *Rev. Sci. Instrum.* **83**, 033507 (2012).

23. Lifschitz, A. *et al.* Ion acceleration in underdense plasmas by ultra-short laser pulses. *New J. Phys.* **16**, 033031 (2014).
24. Sun, G-Z., Ott, E., Lee, Y. C. & Guzdar, P. Self-focusing of short intense pulses in plasmas. *Phys. Fluids* **30**, 526–532 (1987).
25. Fonseca, R. A. *et al.* Osiris: A three-dimensional, fully relativistic particle in cell code for modeling plasma based accelerators. *Lecture Notes Computer Sci.* **2331**, 342–351 (2002).
26. Fonseca, R. A. *et al.* One-to-one direct modeling of experiments and astrophysical scenarios: Pushing the envelope on kinetic plasma simulations. *Plasma Phys. Control. Fusion* **50**, 124034 (2008).
27. Esirkepov, T. Zh., Kato, Y. & Bulanov, S. V. Bow wave from ultraintense electromagnetic pulses in plasmas. *Phys. Rev. Lett.* **101**, 265001 (2008).
28. Kronberg, P. P. Extragalactic magnetic fields. *Rep. Prog. Phys.* **57**(4), 325–382 (1994).

Acknowledgements

The authors acknowledge the support of OSEO project n.I0901001W-SAPHIR, the support of the European Research Council through the PARIS ERC project (contract 226424) and the national research grants BLAN08-1-380251 (GOSPEL) and IS04-002-01

(ILA). A.F. acknowledges collaboration with T. Vinci (LULI, École Polytechnique). The work of J.V. and L.O.S. is partially supported by the European Research Council through the Accelerates ERC project (contract ERC-2010-AdG-267841) and by FCT, Portugal (contract EXPL/FIZ-PLA/0834/1012). We acknowledge PRACE for access to resources on SuperMUC (Leibniz Research Center).

Author contributions

S.K., E.S., M.V. and A.F. conceived, designed and carried out the experimental measurements, A.F. conceived, designed and realized the analysis tools and performed the data analysis, A.L., J.V. and L.O.S. carried out the numerical simulations, A.F., J.V. and L.O.S. wrote the manuscript, V.M. provided overall supervision.

Additional information

Reprints and permissions information is available online at www.nature.com/reprints. Correspondence and requests for materials should be addressed to A.F.

Competing financial interests

The authors declare no competing financial interests.

Methods

High-density micrometric target. The target is a pulsed, high-pressure gas jet system which can drive a sub-millimetric gas nozzle to atomic densities in the range 10^{19} – 10^{21} atoms cm^{-3} (ref. 22).

In our experiment we used a transonic nozzle with an output diameter of 400 μm , producing an expanding flow with a Mach number $M = 1.3$. The radial atomic density profile at a distance of 200 μm from the nozzle level (laser propagation axis) is fitted using $n_A = n_{\text{max}} \exp[-(r/r_0)^{2.1}]$, where $n_{\text{max}} = 3.5 \times 10^{19}$ atoms cm^{-3} and $r_0 = 170 \mu\text{m}$ is the jet radius.

The peak density in the jet decreases exponentially along the vertical direction with a characteristic scale length of $L = 263 \mu\text{m}$.

Probing of the plasma. The plasma is probed by a linearly polarized $\tau_p = 30$ fs, $\lambda = 400$ nm probe pulse synchronized to the main (pump) beam. The probe beam is split into three separate optical set-ups, for simultaneous measurement of density and polar magnetic field.

The radial density map is extracted from the integrated phase of the probe pulse, by means of a Nomarski interferometer on the first transmitted copy of the probe beam. The integrated phase is retrieved by 2D wavelet analysis of the interferogram. The phase map is then normalized by subtraction of a reference phasemap (accounting for aberrations in the laser transport and in the imaging system) and inverted by Hankel–Fourier implementation of the Abel transform.

Magnetic field is retrieved from the polarization rotation φ_{rot} produced on the probe beam by the Faraday effect as

$$\varphi_{\text{rot}} = \frac{e}{2m_e c n_c} \int_l n_0 \mathbf{B} \cdot d\mathbf{z} \quad (1)$$

where $n_c = (2\pi c)^2 m_e \epsilon_0 / e^2 \lambda^2$ is the electron plasma critical density at a wavelength of λ and $d\mathbf{z}$ is the line element along the probe beam propagation (see ref. 29).

To obtain a 2D map of the polarization status in the probe beam profile, the pulse is split into two separate diagnostic lines, each equipped with an analyser and a high dynamic range CCD camera. A total of four images, two with pump and two without, are used for each snapshot of the magnetic field to eliminate effects due to laser intensity fluctuation and systematic optical deformation. The correct superposition of images from the two separate polarization measurement lines is ensured by spatial markers and automated numerical pattern recognition methods.

The map of the polarization rotation $\varphi_{\text{rot}}(x, y)$ is obtained from the ratio between the images recorded by the two ‘Faraday rotation’ CCDs (Fig. 1). Let $I_{p1}(x, y)$ (resp. $I_{p2}(x, y)$) be the plasma shadowgraphy at a polarization angle θ_{p1} (resp. θ_{p2}).

The map of the ratio between the two images $R(x, y) = I_{p1}/I_{p2}(x, y)$ can be written as

$$R(x, y) = \frac{1 - \beta_1 \sin^2 [\pi/2 + \theta_{p1} + \varphi_{\text{rot}}(x, y)]}{1 - \beta_2 \sin^2 [\pi/2 + \theta_{p2} + \varphi_{\text{rot}}(x, y)]}$$

where $\theta_{p1,2}$ are the analysers’ angles and $\varphi_{\text{rot}}(x, y)$ the local polarization rotation. From simple trigonometric operations, having defined $\theta_1 = \pi/2 + \theta_{p1} + \varphi_{\text{rot}}$ and $\Delta_p = \theta_{p2} - \theta_{p1}$, $\varphi_{\text{rot}}(x, y)$ is obtained through

$$\theta_1 = \tan^{-1} \left[\frac{a + (a^2 + b^2 - c^2)^{1/2}}{b + c} \right]$$

where the coefficients are given by

$$\begin{cases} a = R\beta_2 \cos(2\Delta_p) - \beta_1 \\ b = -R\beta_2 \sin(2\Delta_p) \\ c = R\beta_2 - \beta_1 + 2(1 - R) \end{cases}$$

To retrieve the 2D map of the quantity $(n_0 B_\theta)(r, x)$ it is necessary to eliminate the scalar projection in the integral kernel of equation (1). This operation is accomplished via the integral back transform developed in ref. 30:

Table 1 | Laser intensities for the higher order Hermite–Gaussian modes used to fit the experimental laser profile.

| (m, n) | (0, 0) | (0, 1) | (0, 2) | (0, 3) | (0, 4) |
|----------|--------|--------|--------|----------------------|--------|
| a_0 | 2.27 | −0.076 | −0.05 | 6.3×10^{-5} | 0.025 |

$$(n_0 B_\theta)(r, x) = \frac{2m_e c n_c}{\pi e} \frac{\partial}{\partial r} \int_r^{r_0} \frac{\varphi_{\text{rot}}(y, x)}{\sqrt{y^2 - r^2}} dy$$

Owing to the sensitivity of the algorithm, φ_{rot} maps are anti-symmetrized before performing the back transform.

Simulations. Three-dimensional simulations were performed using the fully relativistic particle-in-cell code Osiris^{25,26}, which is routinely used to model laser-wakefield acceleration and astrophysical scenarios.

The particle-in-cell technique (PIC) is a first-principles approach which performs almost no physical approximations as long as quantum effects can be neglected. These simulations therefore include a fully kinetic description of the plasma dynamics, and the self-consistent laser–plasma interaction in relativistic regimes including field ionization of the neutral gas in three dimensions. The initial transverse and longitudinal laser profiles, frequency and focal point, were set to closely follow measured experimental profiles. The initial gas jet density profile measured in experiments was also accurately reproduced in the simulations. The simulations make the following assumptions, which have no influence on the findings: binary collisions are not modelled (a valid assumption in our scenario, which describes collisionless plasmas), impact ionization has not been included (impact ionization is negligible because the probability of hot electron beam electrons ionizing a neutral helium atom is lower than 5×10^{-3}), ions remain immobile (similar simulations including ion motion, but without ionization, showed no differences in results and conclusions).

The simulation window is $1,272 \times 300 \times 300 (\mu\text{m})^3$, divided into $33,000 \times 1,000 \times 1,000$ cells with $2 \times 1 \times 1$ particles per cell, giving a total of 6.6×10^{10} simulation particles and a total simulation time between 200,000 and 400,000 CPUh. Simulations considered an initial helium gas jet density profile given by $n_0 = 3.5 \times 10^{19} \text{ cm}^{-3} \exp[|x - 700 \mu\text{m}|/340 \mu\text{m}]^{2.1}$, x being the longitudinal position in microns, which reproduces the experimental conditions. Ionization was modelled using ADK tunnel ionization rates. The longitudinal profile of the laser electric field is symmetric and given by $10\tau^3 - 15\tau^4 + 6\tau^5$, with $\tau = \sqrt{2}t/\tau_{\text{FWHM}}$, where τ_{FWHM} is the FWHM duration of the laser pulse. The transverse laser profile is a fit to a transverse line taken from the experimental laser intensity profile using higher-order Hermite–Gaussian modes. Given $r = \sqrt{(y^2 + z^2)}$ the distance to the propagation axis, each mode electric field profile is defined as:

$$E(x) = \frac{E_0}{W(x)} H_n \left(\frac{y\sqrt{2}}{W(x)} \right) H_m \left(\frac{z\sqrt{2}}{W(x)} \right) \exp \left(\frac{-r^2}{W(x)^2} \right) \times \cos \left[k_0 x + \frac{k_0 r^2 x}{2(x^2 + Z_p^2)} - \zeta_{mn}(x) \right]$$

where E_0 is the peak electric field, $k_0 = \omega_0/c$, $\omega_0 = 2.34 \times 10^{15}$ radian s^{-1} is the laser frequency corresponding to a central laser wavelength of 800 nm, $\zeta_p(x) = (m + n + 1) \tan^{-1}(x/Z_p)$ is the Gouy phase shift, $Z_p = k_0 W_0^2/2$ is the Rayleigh length, $W(x)^2 = W_0^2(1 + x^2/Z_p^2)$, and H_n the n th-order Hermite polynomial. Table 1 shows the laser peak normalized vector potentials (a_0) of the five higher-order Gaussian beams associated with the fit to the experimental laser profile. A value of $W_0 = 9.8 \mu\text{m}$ was used.

References

- Buck, A. *et al.* Real-time observation of laser-driven electron acceleration. *Nature Phys.* **7**, 1745–1747 (2011).
- Flacco, A., Rax, J.-M. & Malka, V. Reconstruction of polar magnetic field from single axis tomography of Faraday rotation in plasmas. *Phys. Plasmas* **19**, 103107 (2012).